nature communications

Article

https://doi.org/10.1038/s41467-024-53882-2

A single-photon emitter coupled to a phononic-crystal resonator in the resolved-sideband regime

Received: 11 August 2024

Accepted: 25 October 2024

Published online: 04 November 2024

Check for updates

Clemens Spinnler[1] ✉, Giang N. Nguyen[1], Ying Wang[2], Liang Zhai[1,4], Alisa Javadi[1,5], Marcel Erbe[1], Sven Scholz[3], Andreas D. Wieck[3], Arne Ludwig[3], Peter Lodahl[2], Leonardo Midolo[2] & Richard J. Warburton[1]

A promising route towards the deterministic creation and annihilation of single-phonons is to couple a single-photon emitter to a mechanical resonator. The challenge lies in reaching the resolved-sideband regime with a large coupling rate and a high mechanical quality factor. We achieve this by coupling self-assembled InAs quantum dots to a small mode-volume phononic-crystal resonator with mechanical frequency $\Omega_m/2\pi$ = 1.466 GHz and quality factor $Q_m = 2.1 \times 10^3$. Thanks to the high coupling rate of $g_{ep}/2\pi$ = 2.9 MHz, and by exploiting a matching condition between the effective Rabi and mechanical frequencies, we observe the interaction between the two systems via correlations in the emitted photons. Our results represent a major step towards quantum control of the mechanical resonator via a single-photon emitter.

Coupling a quantum system to a mechanical resonator is of both fundamental and technological interest. A highly studied area is the use of photons to control the state of a mechanical system[1]. To enhance the interaction, cavities have been introduced in the form of two mirrors facing each other[2], ring resonators[3], photonic crystals[4], and microwave resonators[5]. Additionally, various quantum systems have been coupled to mechanical resonators, for instance superconducting qubits[6], atomic ensembles[7], and solid-state emitters[8].

For phononic quantum technologies[9], it becomes necessary to create one phonon at a time[10]. Using optical cavities, this is achieved with a highly attenuated laser pulse; the phonon creation is probabilistic with a probability much below one[10]. An alternative approach is to use a single-photon emitter in the resolved sideband regime. With π-pulse excitation on the blue sideband, phonons can be created on demand. The advantage of the single-emitter is that it breaks the harmonicity of the cavity's photon ladder. Furthermore, the theory has shown that the single emitter itself can be used to laser-cool the mechanical system to its ground state[11].

To date, different kinds of single-photon emitters have been coupled to mechanical resonators: colour centres[12,13], rare-earth ions[14], 2D-materials[15], and quantum dots[8,16–29]. So far, the sensitivity to mechanical motion is low and the interaction between the two systems was probed by driving the mechanical resonator, i.e., by adding phonons. However, to explore single-phonon applications, it is crucial to operate in the few-phonon regime, ultimately in the quantum ground state[30].

Semiconductor quantum dots (QDs) are excellent emitters of high-quality single-photons[31–34]. The upper level, the exciton, couples to lattice vibrations via a strain-induced deformation potential[11,22,35]. In the resolved-sideband regime, the angular frequency of the mechanical resonance, Ω_m, must be larger than the radiative decay rate of the QD exciton, Γ_R. In addition, for optical driving of the phonon sidebands, it is important that Ω_m is also larger than the inhomogeneously-broadened linewidth, Γ_{inh}[36]. Satisfying these two conditions is challenging for many reasons. First, the mechanical frequencies need to be in the gigahertz regime, where mechanical loss rates tend to be high[37]. Second, obtaining narrow optical linewidths (i.e., small

[1]Department of Physics, University of Basel, Basel, Switzerland. [2]Center for Hybrid Quantum Networks (Hy-Q), The Niels Bohr Institute, University of Copenhagen, Copenhagen Ø, Denmark. [3]Lehrstuhl für Angewandte Festkörperphysik, Ruhr-Universität Bochum, Bochum, Germany. [4]Present address: Institute of Fundamental and Frontier Sciences, University of Electronic Science and Technology of China, Chengdu, PR China. [5]Present address: School of Electrical and Computer Engineering, University of Oklahoma, Norman, OK, USA. ✉e-mail: c.spinnler@unibas.ch

inhomogeneous broadening) on QDs embedded in mechanical resonators can be difficult[35]. Third, for high exciton-phonon coupling rates, the mechanical resonator size needs to be small such that the implementation of a phononic shield becomes necessary[38].

In this work, we face the aforementioned challenges by coupling self-assembled InAs QDs[39] to a phononic-crystal resonator (PnCR) with $\Omega_m/2\pi = 1.466$ GHz and $Q_m = 2.1 \times 10^3$. We achieve narrow optical linewidths and hence a high sensitivity of the QD's optical response to the mechanics. We drive the QD's optical transition resonantly and analyse the emitted photons using quantum optics techniques. Specifically, a measurement of the auto-correlation function reveals the mechanical motion when the effective Rabi frequency matches the mechanical resonance frequency. We detect the interaction of a quantum emitter and a mechanical resonator in the few-phonon regime with $\langle n_m \rangle = 58$ (thermal motion at 4.2 K) and extract a state-of-the-art exciton-phonon coupling rate of $g_{ep}/2\pi = 2.9$ MHz.

Results

Sample design and characterisation

The mechanical resonator is etched into a 180 nm GaAs membrane. The membrane hosts InAs QDs; the QDs are embedded in a p-i-n diode, see inset to Fig. 1a[40–42]. Figure 1a, b shows finite-element simulations of the PnCR. The mechanical in-plane breathing mode is tightly confined by the phononic bandgap structure[38] and shows a highly homogeneous strain profile in the centre of the resonator (see Supplementary Note 1). The PnCR consists of seven holes (phononic-shield unit cells) etched into the membrane[40], see Fig. 2a. Due to the small beam cross-section (960×180 nm^2), the breathing mode has a mode volume as small as $4 \times 10^{-3}\lambda^3$ (with $\lambda = 3.25$ µm). As a result, our simulations predict a low effective mass $m_{eff} = 7.4 \times 10^{-16}$kg, a large zero-point motion $x_{zpf} = 2.7 \times 10^{-15}$m, and a high exciton-phonon coupling rate $g_{ep}^{sim}/2\pi = 3.2$ MHz (see Supplementary Note 1). The thermal phonon occupation of the breathing mode is $\langle n_m \rangle = 58$ at 4.2 K. The PnCR does not support an optical cavity but this could be included in subsequent designs.

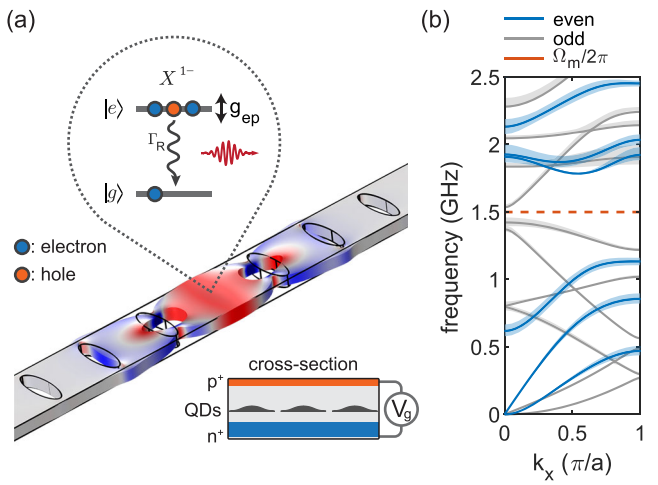

Fig. 1 | Finite-element simulations of a quantum dot coupled to a mechanical resonator. a Phononic-crystal resonator hosting a semiconductor diode-structure for quantum dot (QD) charge control (see cross-section). The QD emits single photons and its excited state is dispersively coupled to the mechanical motion via a deformation potential (example given for the negative trion X^{1-}). The resonator consists of a well-isolated mechanical mode at $\Omega_m/2\pi \approx 1.5$ GHz tightly confined by the surrounding phononic shield. **b** Band diagram of the phononic shield. The width of the bandgap is 0.65 GHz and 0.11 GHz for even and odd modes in terms of the *z*-symmetry, respectively. Shaded areas represent band broadening upon varying the air-hole parameters by ±20 nm.

We select a QD with a potentially large exciton-phonon coupling rate from a photoluminescence map[37,43]. Figure 2b shows several bright QDs located around the centre of the beam. Switching to resonant excitation of a single QD, a plateau map of the negative trion X^{1-} is recorded, see Fig. 2c. Upon changing the applied gate voltage, V_g, the emission frequency is tuned (via the dc Stark effect) over a frequency range of more than 50 times the QD's linewidth. The lifetime of the excited state is extracted from a pulsed measurement $\tau_R = 1.18$ ns, which corresponds to a radiative decay rate of $\Gamma_R = 2\pi \times 135$ MHz (see Supplementary Note 3). On account of the diode structure and optimised nano-fabrication, we obtain narrow optical linewidths, here, a factor of four above the transform limit $\Gamma_{inh} = 4\Gamma_R$, see Fig. 2d.

Exciton-phonon interaction

In the absence of an optical cavity, the only way to detect the mechanical motion is via the QD. It is crucial to consider how the exciton-phonon coupling can be measured, in particular, the coupling to mechanical oscillations driven only by thermal noise (i.e., the Brownian motion).

In the unresolved-sideband regime, mechanical noise results in fluctuations in the intensity of the resonance fluorescence[35]. The relative sensitivity is proportional to the square of the normalised derivative of the resonance fluorescence counts (with respect to laser detuning), see Fig. 3b. The highest sensitivity is obtained at low excitation power and laser detunings corresponding to half the optical linewidth[35]. In the resolved sideband regime, this technique fails. The mechanical resonator oscillates back and forth several times during the exciton lifetime, resulting in acoustic sidebands at $\Delta\omega_l = \pm\,\Omega_m$[37], such that the resonance fluorescence intensity becomes insensitive to the mechanical motion.

An alternative scheme relies on driving the system at a resonance condition close to the mechanical sidebands. The quantum dot is driven with frequency detuning $\Delta\omega_l/2\pi$ and Rabi coupling Ω_R. The field created by the QD oscillates at the effective Rabi frequency, $\Omega_R^{eff}/2\pi$, where $\Omega_R^{eff} = \sqrt{\Omega_R^2 + \Delta\omega_l^2}$. The resonance condition is that the effective Rabi frequency should match the mechanical resonance frequency, $\Omega_m/2\pi$, i.e., $\Omega_R^{eff} = \Omega_m$[44]. Fulfilling this condition, the mechanical motion becomes visible in the auto-correlation function of the emitted photons.

To analyse this resonance precisely, we simulate a driven two-level system with parameters appropriate to our system. The mechanical coupling is introduced via a frequency shift of the upper level, here the trion. The model is semi-classical: the two-level system is treated quantum mechanically; both the laser drive and the mechanics are treated classically. We assume that the mechanical phase is static with respect to the time dynamics of the quantum emitter[45,46]. To obtain the time-dependent mechanical backaction on the excited-state population, we solve the master equations numerically. Specifically, we simulate the sensitivity of the resonance fluorescence to the mechanical motion, $\int S_{nn}(f_m)df$ (where S_{nn} is the noise-power spectrum), as a function of laser detuning and Rabi coupling, Fig. 3c. As expected, the sensitivity is zero at small detunings and at small Rabi couplings yet large at the resonance condition.

A qualitative understanding of the resonance condition, i.e., the sensitivity resonances in Fig. 3c, can be found in the dressed-state picture. Figure 3a shows the phonon-ladder diagram where neighbouring ground and excited states are separated by the phonon energy $\hbar\Omega_m$ (orange arrows). Vertical transitions correspond to transitions which conserve the phonon number of the resonator (elastic scattering), and diagonal transitions change the phonon population by ± 1 (Stokes/anti-Stokes scattering). The optical excitation dresses the energy levels of the quantum emitter and splits them by an energy $\hbar\Omega_R^{eff} = \hbar\sqrt{\Omega_R^2 + \Delta\omega_l^2}$ (blue arrows). The sensitivity of the QD to the

mechanical resonator is strongest whenever a combination of Ω_R and $\Delta\omega_l$ is chosen such that $\Omega_R^{eff} = \Omega_m$[44]. In the dressed-state picture, the condition $\Omega_R^{eff} = \Omega_m$ means that states involving different phonon numbers are degenerate and mechanical quanta can be exchanged

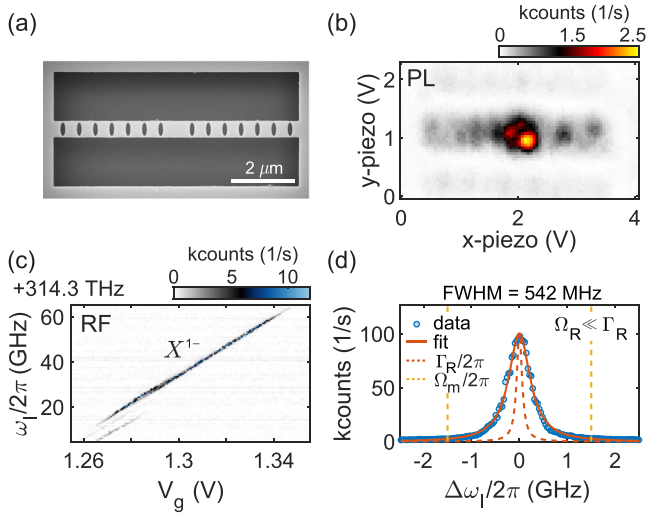

Fig. 2 | Quantum dot characterisation. a Scanning electron-microscope image of the fabricated device with seven shield elements on each side. **b** Photoluminescence (PL) map showing several QDs in the centre of the phononic-crystal beam. **c** Resonance fluorescence (RF) charge-plateau scan of the negative trion (X^{1-}) of a QD close to the resonator's centre. **d** Low-power frequency scan to determine the inhomogeneously-broadened linewidth, $\Gamma_{inh}/2\pi = 550$ MHz. The data are fitted to a Lorentzian. The transform limit ($\Gamma_R/2\pi$) and the sideband position ($\Delta\omega_l = \pm\,\Omega_m$) are shown.

without the cost of energy (black arrows).This picture applies specifically to a two-level system and not to a harmonic system such as a cavity for which there is a ladder of excited states. In cavity optomechanics, the resonance condition is simply $\Delta\omega_l = \Omega_m$ and is independent of the laser power.

At low excitation powers ($\Omega_R \ll \Gamma_m$) the resonance condition implies detuning the laser to the blue or red sideband. At high excitation powers ($\Omega_R > \Gamma_m$), the laser detuning needs to be smaller than the mechanical frequency. Above $\Omega_R > \Omega_m$ ($\Omega_m = 10.8\Gamma_R$ here), the resonance condition can no longer be met and the sensitivity is therefore small. The signal-to-noise ratio increases with higher QD counts, and the simulation shows that there is a maximum around $\Omega_R \approx 8\Gamma_R$ (see Supplementary Note 5).

Detection of thermal motion

The simulations motivate the choice of Ω_R^{eff} in the experiment. We perform two individual measurements with parameter sets (Rabi frequency and laser detuning) (I) $\Omega_R^{eff} < \Omega_m$ and (II) $\Omega_R^{eff} = \Omega_m$. Here, Ω_m is the mechanical frequency expected from the simulations. The measurements are performed at $\Omega_R = 4\Gamma_R$, where the linewidth is just slightly power broadened. Ω_R is calibrated with a power series measurement (see Supplementary Note 3). Figure 3d shows the associated linewidth scan. Due to the high optical power, the background level (unsuppressed laser) increases. For (I) the laser detuning corresponds to $\Delta\omega_l/2\pi$ = 0.5 GHz (yellow line) and for (II) $\Delta\omega_l/2\pi = 1.4$ GHz (green line).

To probe the QD-mechanical interaction we record 8 h of auto-correlation data while repeatedly suppressing the laser and correcting for a small spectral drift (see Supplementary Note 3). Figure 3e shows the auto-correlation measurements for (I) and (II). Close to zero delays, Rabi oscillations of $\Omega_R^{eff}/2\pi$ are visible, with frequencies matching those expected from the calibration. The dip at $\tau = 0$ (a measure of the single-photon purity) reaches values far from zero on account of the increased laser background (see Fig. 3d and Supplementary Note 3). The noise-power spectrum, S_{nn}, is obtained from the auto-correlation measurement via Fourier transform (see Supplementary Note 4)[35]. Figure 3f shows S_{nn} for configurations (I) and (II) obtained from an auto-correlation with a maximum time delay of τ_{max} = 500 ns and time binning of τ_{bin} = 50 ps. In case (II) (green spectra), a prominent peak is visible at a frequency of 1.466 GHz. In case (I) (yellow spectra), no peaks are visible, although the click rate on the detectors is much higher and the noise floor is much lower than for (II).

We identify the peak at 1.466 GHz as the mechanical resonance on two grounds. First, S_{nn} follows the dependence on Ω_R^{eff} as predicted by the simulations. Second, the frequency at the peak, 1.466 GHz, lies very close to the mechanical resonance frequency obtained from finite-element simulations, 1.496 GHz. Thus, the coupled hybrid system is in the resolved-sideband regime with $\Omega_m \approx 11\Gamma_R$ but more importantly $\Omega_m \approx 2.7\Gamma_{inh}$.

The inset to Fig. 3f displays the mechanical noise-peak with high resolution (FFT of auto-correlation with τ_{max} = 8 μs and τ_{bin} = 50ps). A mechanical quality factor as high as $Q_m = 2.1 \times 10^3$ is extracted via a Lorentzian fit. This justifies the assumption in the simulations that the mechanical damping rate is much less than than the QD's radiative decay rate.

Exciton-phonon coupling rate

To estimate the exciton-phonon coupling rate, $g_{ep} = (\delta\omega_{QD}/\delta x) \cdot x_{zpf}$, we perform the noise-power measurement upon sweeping the laser detuning (at fixed laser power). We chose $\Omega_R = 8\Gamma_R$, for which the highest interaction between the two systems is expected at $\Delta\omega_l/2\pi = 1.0$ GHz. Figure 3g shows the integrated noise power versus laser detuning. For each data point, 1 h of auto-correlation data are recorded. Via a model fit to the data, an exciton-phonon coupling strength of $g_{ep}/2\pi = 2.9$ MHz is extracted. This agrees very well with the simulated value, 3.2 MHz. Finally, we repeat the auto-correlation measurement with optimised parameters for the highest signal-to-noise ratio, see Fig. 3h. The oscillations due to the interaction with the mechanical resonator now become visible, even without a Fourier transform.

A prominent feature of the noise spectra, Fig. 3f, is that only one peak is observed. Furthermore, both the mechanical frequency and the coupling $g_{ep}/2\pi$ are very close to the simulated values. These observations show that the phononic resonator operates as per design: modes in the gap are both decoupled from the environment via the phononic shield and highly confined to the central island. The many mechanical modes lying outside the bandgap are highly damped and are therefore not observed. Considering that the phononic shield works well, it is likely that the mechanism limiting the mechanical quality factor is related to damping mechanisms within the material. Notably, GaAs gigahertz-frequency mechanical resonators with mechanical quality factors exceeding 10^4 have been achieved[8,47]. This suggests that the present mechanical quality factor is limited by surface losses and/or losses within the doped regions. One approach to reduce these losses could be surface passivation[48–50]. Moreover, the quality factor could also be enhanced via soft clamping and further strain engineering[51,52].

Discussion

The figure of merit for the mechanical signal strength is the thermal coupling rate normalised to the mechanical angular frequency, g_{ep}^{th}/Ω_m with $g_{ep}^{th} = g_{ep}\sqrt{2\langle n_m \rangle}$. To enhance the signal strength, it is important to improve g_{ep} further without increasing the mechanical frequency. This can be achieved by either reducing the width of the beam and thus the effective mass ($g_{ep} \propto m_{eff}^{-1/2}$), or by choosing a two-dimensional resonator design hosting a degenerate breathing mode.

https://doi.org/10.1038/s41467-024-53882-2

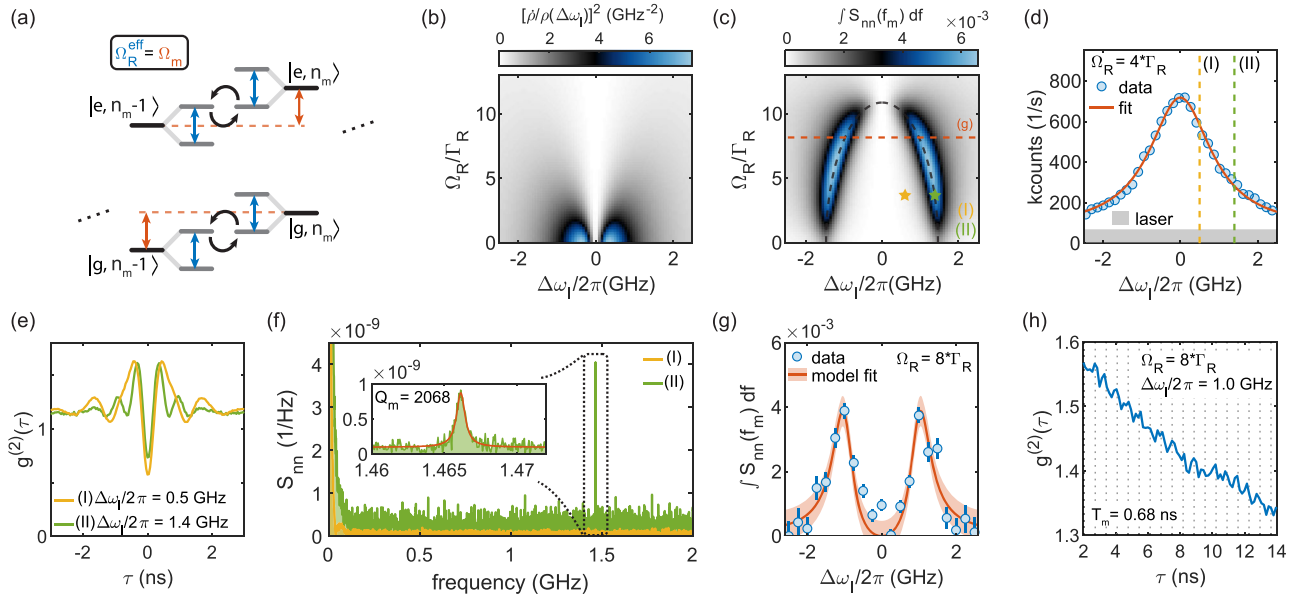

Fig. 3 | Exciton-phonon coupling strength. a Phonon-energy-ladder diagram for a driven two-level system. The excitation laser dresses the two-level system. The interaction between the two systems is strongest when the dressed-state splitting (effective Rabi frequency, $\Omega_R^{\mathrm{eff}}/2\pi$) is equal to the sideband separation (mechanical frequency, $\Omega_m/2\pi$). **b** Simulated mechanical-noise sensitivity in the unresolved-sideband regime, given by the derivative of the QD counts. **c** Simulated mechanical-noise sensitivity of the current device. $\int S_{nn}(f_m)df$ is the integrated noise power of the mechanical resonace. The condition of $\Omega_R^{\mathrm{eff}} = \Omega_m$ is highlighted by the dashed black line. **d** QD linewidth at elevated excitation power ($\Omega_R = 4\Gamma_R$) as used in the thermal-motion measurement. **e** Auto-correlation measurements at two different detunings (i) and (ii) (see dashed lines in (**d**) and stars in (**c**)). The larger detuning corresponds to $\Omega_R^{\mathrm{eff}} = \Omega_m$. **f** Noise-power spectra obtained from (**e**) reveal the mechanical peak only for optimal effective Rabi frequency (detuning (ii), green line). **g** Integrated mechanical noise in dependence on the laser detuning. An exciton-phonon coupling rate of $g_{ep}/2\pi = 2.9$ MHz is extracted from a model-fit to the data. Data and fit errors are given by one standard deviation. **h** Zoom-in of a 14-h auto-correlation measurement, showing mechanical oscillations. Dashed lines show the expected noise peaks, spaced by $T_m = 2\pi/\Omega_m = 0.68$ns.

For single-phonon experiments, it is crucial to reach below $\langle n_m \rangle = 1$. To estimate the backaction on the mechanical resonator, we perform additional simulations in which the mechanical resonator is described in a fully quantum way with decay to a thermal bath (see Supplementary Note 5). Also here, the strongest interaction is found when $\Omega_R^{\mathrm{eff}} = \Omega_m$. Currently, the change in phonon number that we achieve with red-detuned driving is too small (below two, see Supplementary Note 5) to be detectable in the auto-correlation measurement. The cooling performance can be improved by increasing the mechanical quality factor, reducing the inhomogeneous broadening, and by increasing the coupling rate. At 4.2 K, a measurable change in phonon population could be achieved with the present system via a five-fold increase in the mechanical quality factor ($Q_m = 10^4$). However, the lowest phonon number would still be much above one (see Supplementary Note 5). An alternative approach is to start at a bath temperature of 100mK where $\langle n_m \rangle = 0.98$. With a five-fold enhanced Q_m, a two-fold increased g_{ep}, and a transform-limited linewidth[53], the lowest phonon occupation that can be reached is $\langle n_m \rangle = 0.56$, a suitable starting point for single-phonon experiments.

In summary, we present a QD coupled to a phononic-crystal resonator in the resolved-sideband regime. Upon resonant excitation, the QD has a narrow optical linewidth and a high mechanical sensitivity. We demonstrate that the interaction between the two systems is strongest when matching the eigenfrequency of the dressed QD with the mechanical frequency: $\Omega_R^{\mathrm{eff}} = \Omega_m$. Satisfying this condition allows us to observe even the thermally-driven mechanical oscillations (at 4.2 K) and to determine precisely the mechanical resonator's frequency. Via the noise power spectrum, we determine the exciton-phonon coupling, $g_{ep}/2\pi = 2.9$ MHz (an unprecedentedly high value), and the mechanical quality factor, 2.1×10^3. The low mechanical damping rate results in a high $Q_m \cdot f_m$ product of 3.0×10^{12} Hz, which allows for 34 mechanical oscillations before coherence is lost.

As an outlook, we mention that cooling the present device to millikelvin temperatures is sufficient to reach $\langle n_m \rangle < 1$. Cooling (and heating) of the mechanical resonator via optical driving of the QD should become possible with slightly improved device parameters. Furthermore, several QDs can be included in the same mechanical resonator facilitating a coherent exciton-exciton coupling. There are prospects of coupling the spin to the mechanical motion in a similar phononic resonator: this also allows deterministic single-phonon creation, in this case via spin relaxation[54], and potentially facilitates a coherent coupling between spins in separate QDs.

Data availability

The data that supports this work is available from the corresponding author upon request.

Code availability

The code used for this work is available from the corresponding author upon request.

References

1. Aspelmeyer, M., Kippenberg, T. J. & Marquardt, F. Cavity optomechanics. *Rev. Mod. Phys.* **86**, 1391–1452 (2014).
2. Thompson, J. D. et al. Strong dispersive coupling of a high-finesse cavity to a micromechanical membrane. *Nature* **452**, 72–75 (2008).
3. Verhagen, E., Deléglise, S., Weis, S., Schliesser, A. & Kippenberg, T. J. Quantum-coherent coupling of a mechanical oscillator to an optical cavity mode. *Nature* **482**, 63–67 (2012).
4. Chan, J. et al. Laser cooling of a nanomechanical oscillator into its quantum ground state. *Nature* **478**, 89–92 (2011).
5. Teufel, J. D. et al. Sideband cooling of micromechanical motion to the quantum ground state. *Nature* **475**, 359–363 (2011).
6. Chu, Y. et al. Quantum acoustics with superconducting qubits. *Science* **358**, 199–202 (2017).

7. Karg, T. M. et al. Light-mediated strong coupling between a mechanical oscillator and atomic spins 1 meter apart. *Science* **369**, 174–179 (2020).
8. DeCrescent, R. A. et al. Large single-phonon optomechanical coupling between quantum dots and tightly confined surface acoustic waves in the quantum regime. *Phys. Rev. Appl.* **18**, 034067 (2022).
9. Barzanjeh, S. et al. Optomechanics for quantum technologies. *Nat. Phys.* **18**, 15–24 (2022).
10. Riedinger, R. et al. Non-classical correlations between single photons and phonons from a mechanical oscillator. *Nature* **530**, 313–316 (2016).
11. Wilson-Rae, I., Zoller, P. & Imamoglu, A. Laser cooling of a nanomechanical resonator mode to its quantum ground state. *Phys. Rev. Lett.* **92**, 075507 (2004).
12. Lee, K. W. et al. Strain coupling of a mechanical resonator to a single quantum emitter in diamond. *Phys. Rev. Appl.* **6**, 034005 (2016).
13. Cady, J. V. et al. Diamond optomechanical crystals with embedded nitrogen-vacancy centers. *Quantum Sci. Technol.* **4**, 024009 (2019).
14. Ohta, R. et al. Rare-earth-mediated optomechanical system in the reversed dissipation regime. *Phys. Rev. Lett.* **126**, 047404 (2021).
15. Patel, S. D. et al. Surface acoustic wave cavity optomechanics with WSe_2 single-photon emitters. *PRX Quantum* **5**, 010330 (2024).
16. Carter, S. G. et al. Spin-mechanical coupling of an inas quantum dot embedded in a mechanical resonator. *Phys. Rev. Lett.* **121**, 246801 (2018).
17. Carter, S. G. et al. Tunable coupling of a double quantum dot spin system to a mechanical resonator. *Nano Lett.* **19**, 6166–6172 (2019).
18. Yuan, X. et al. A frequency-tunable nanomembrane mechanical oscillator with embedded quantum dots. *Appl. Phys. Lett.* **115**, 6166–6172 (2019).
19. Vogele, A. et al. Quantum dot optomechanics in suspended nanophononic strings. *Adv. Quantum Technol.* **3**, 1900102 (2020).
20. Montinaro, M. et al. Quantum dot opto-mechanics in a fully self-assembled nanowire. *Nano Lett.* **14**, 4454–4460 (2014).
21. Descamps, T. et al. Dynamic strain modulation of a nanowire quantum dot compatible with a thin-film lithium niobate photonic platform. *ACS Photonics* **10**, 3691–3699 (2023).
22. Yeo, I. et al. Strain-mediated coupling in a quantum dot-mechanical oscillator hybrid system. *Nat. Nanotechnol.* **9**, 106–110 (2014).
23. Yeo, I., Kim, H. J., Song, J. D. & Yi, K. S. Hybrid quantum optomechanics with a quantum-dot single photon source. *Phys. Rev. B* **94**, 165422 (2016).
24. de Assis, P.-L. et al. Strain-gradient position mapping of semiconductor quantum dots. *Phys. Rev. Lett.* **118**, 117401 (2017).
25. Kettler, J. et al. Inducing micromechanical motion by optical excitation of a single quantum dot. *Nat. Nanotechnol.* **16**, 283–287 (2021).
26. Finazzer, M. et al. On-chip electrostatic actuation of a photonic wire antenna embedding quantum dots. *Nano Lett.* **23**, 2203–2209 (2023).
27. Carter, S. G. et al. Sensing flexural motion of a photonic crystal membrane with InGaAs quantum dots. *Appl. Phys. Lett.* **111**, 183101 (2017).
28. Nysten, E. D. S., Rastelli, A. & Krenner, H. J. A hybrid (Al)GaAs-LiNbO3 surface acoustic wave resonator for cavity quantum dot optomechanics. *Appl. Phys. Lett.* **117**, 121106 (2020).
29. Imany, P. et al. Quantum phase modulation with acoustic cavities and quantum dots. *Optica* **9**, 501–504 (2022).
30. O'Connell, A. D. et al. Quantum ground state and single-phonon control of a mechanical resonator. *Nature* **464**, 697–703 (2010).
31. Senellart, P., Solomon, G. & White, A. High-performance semiconductor quantum-dot single-photon sources. *Nat. Nanotechnol.* **12**, 1026–1039 (2017).
32. Lodahl, P., Ludwig, A. & Warburton, R. J. A deterministic source of single photons. *Phys. Today* **75**, 44–50 (2022).
33. Zhai, L. et al. Low-noise GaAs quantum dots for quantum photonics. *Nat. Commun.* **11**, 4745 (2020).
34. Zhai, L. et al. Quantum interference of identical photons from remote GaAs quantum dots. *Nat. Nanotechnol.* **17**, 829–833 (2022).
35. Munsch, M. et al. Resonant driving of a single photon emitter embedded in a mechanical oscillator. *Nat. Commun.* **8**, 76 (2017).
36. Spinnler, C. et al. Quantum dot coupled to a suspended-beam mechanical resonator: from the unresolved- to the resolved-sideband regime. *Phys. Rev. Appl.* **21**, 034046 (2024).
37. Spinnler, C. Exploiting phonon and Coulomb interactions in semiconductor quantum dots. *PhD Thesis, University of Basel* (2023).
38. Safavi-Naeini, A. H. & Painter, O. Design of optomechanical cavities and waveguides on a simultaneous bandgap phononic-photonic crystal slab. *Opt. Express* **18**, 14926–14943 (2010).
39. Löbl, M. C. et al. Excitons in InGaAs quantum dots without electron wetting layer states. *Commun. Phys.* **2**, 1–7 (2019).
40. Midolo, L., Pregnolato, T., Kiršanskė, G. & Stobbe, S. Soft-mask fabrication of gallium arsenide nanomembranes for integrated quantum photonics. *Nanotechnology* **26**, 484002 (2015).
41. Löbl, M. C. et al. Narrow optical linewidths and spin pumping on charge-tunable close-to-surface self-assembled quantum dots in an ultrathin diode. *Phys. Rev. B* **96**, 165440 (2017).
42. Ludwig, A. et al. Ultra-low charge and spin noise in self-assembled quantum dots. *J. Cryst. Growth* **477**, 193–196 (2017).
43. Löbl, M. C. et al. Correlations between optical properties and Voronoi-cell area of quantum dots. *Phys. Rev. B* **100**, 155402 (2019).
44. Rabl, P. Cooling of mechanical motion with a two-level system: the high-temperature regime. *Phys. Rev. B* **82**, 165320 (2010).
45. Weiß, M. et al. Optomechanical wave mixing by a single quantum dot. *Optica* **8**, 291–300 (2021).
46. Wigger, D. et al. Resonance-fluorescence spectral dynamics of an acoustically modulated quantum dot. *Phys. Rev. Res.* **3**, 033197 (2021).
47. Forsch, M. et al. Microwave-to-optics conversion using a mechanical oscillator in its quantum ground state. *Nat. Phys.* **16**, 69–74 (2020).
48. Kuruma, K., Ota, Y., Kakuda, M., Iwamoto, S. & Arakawa, Y. Surface-passivated high-Q GaAs photonic crystal nanocavity with quantum dots. *APL Photonics* **5**, 046106 (2020).
49. Najer, D. et al. Suppression of surface-related loss in a gated semiconductor microcavity. *Phys. Rev. Appl.* **15**, 044004 (2021).
50. Chan, J. Laser cooling of an optomechanical crystal resonator to its quantum ground state of motion. *PhD Thesis, California Institute of Technology* (2012).
51. Tsaturyan, Y., Barg, A., Polzik, E. S. & Schliesser, A. Ultracoherent nanomechanical resonators via soft clamping and dissipation dilution. *Nat. Nanotechnol.* **12**, 776–783 (2017).
52. Ghadimi, A. H. et al. Elastic strain engineering for ultralow mechanical dissipation. *Science* **360**, 764–768 (2018).
53. Pedersen, F. T. et al. Near transform-limited quantum dot linewidths in a broadband photonic crystal waveguide. *ACS Photonics* **7**, 2343–2349 (2020).
54. Söllner, I., Midolo, L. & Lodahl, P. Deterministic single-phonon source triggered by a single photon. *Phys. Rev. Lett.* **116**, 234301 (2016).

Acknowledgements

We thank Martino Poggio, Tomasz A. Jakubczyk, Yannik Laurent Fontana, Hinrich Mattiat, Thibaud Ruelle, and Guillaume Bertel for stimulating discussions. The work was supported by SNF Project 200020_204069. G.N.N., M.E., L.Z., and A.J. received funding from the European Union's Horizon 2020 Research and Innovation Programme under the Marie Skłodowska-Curie grant agreement No. 861097 (QUDOT-TECH), No.

721394 (4PHOTON), and No. 840453 (HiFig), respectively. Y.W., P.L. and L.M. acknowledge financial support from Danmarks Grundforskningsfond (DNRF 139, Hy-Q Centre for Hybrid Quantum Networks). L.M. acknowledges the European Research Council (ERC) under the European Union's Horizon 2020 research and innovation programme (Grant Agreement No. 949043, NANOMEQ). S.S., A.D.W. and A.L. acknowledge financial support from the grants DFH/UFA CDFA05-06, DFG TRR160, DFG project 383065199, and BMBF Q.Link.X 16KIS0867.

Author contributions

S.S., A.D.W. and A.L. designed and grew the QD sample. C.S., L.Z., G.N.N., A.J. and R.J.W. designed the mechanical structures following the scheme developed by P.L. and L.M.; Y.W., L.M., and P.L. fabricated the mechanical structures. C.S. and L.Z. performed the simulations. C.S., G.N.N., L.Z., A.J., M.E. and R.J.W. carried out the experiments and analysed the data. C.S., G.N.N. and R.J.W. wrote the manuscript with input from all the authors.

Competing interests

The authors declare no competing interests.

Additional information

Supplementary information The online version contains supplementary material available at https://doi.org/10.1038/s41467-024-53882-2.

Correspondence and requests for materials should be addressed to Clemens Spinnler.

Peer review information *Nature Communications* thanks the anonymous reviewer(s) for their contribution to the peer review of this work. A peer review file is available.